Available online at www.sciencedirect.com

jmr&t Journal of Materials Research and Technology

journal homepage: www.elsevier.com/locate/jmrt

Original Article

Recrystallization and grain growth kinetics of IN718 manufactured by laser powder bed fusion

Merve Nur Doğu [a,b,c,*], *Kemal Davut* [d], *Muhannad Ahmed Obeidi* [a,b,c], *Mustafa Alp Yalçın* [e], *Hengfeng Gu* [f], *Thaddeus Song En Low* [f], *Jon Ginn* [f], *Dermot Brabazon* [a,b,c]

[a] *I-Form Advanced Manufacturing Research Centre, Dublin City University, Dublin, Ireland*
[b] *School of Mechanical & Manufacturing Engineering, Dublin City University, Dublin, Ireland*
[c] *Advanced Processing Technology Research Centre, Dublin City University, Dublin, Ireland*
[d] *Department of Materials Science and Engineering, Izmir Institute of Technology, 35430, Urla, Izmir, Turkey*
[e] *Metal Forming Center of Excellence, Atılım University, Ankara, Turkey*
[f] *Ansys Inc., 1441 W Ute Blvd, Suite 335, Park City, UT 84098, USA*

ARTICLE INFO

Article history:
Received 17 May 2022
Accepted 29 June 2022
Available online 2 July 2022

Keywords:
IN718
Laser powder bed fusion
Solution heat treatment
Microstructure
Texture
Recrystallization
Electron backscatter diffraction

ABSTRACT

The recrystallization and grain growth behaviour of IN718 alloy additively manufactured by laser powder bed fusion (L-PBF) is presented herein. The effects of three different temperatures (1050, 1150 and 1250 °C) and holding times (15, 45 and 90 min) were investigated. The texture evolution of the samples was recorded via electron backscatter diffraction (EBSD). The as-built sample is composed of bowl-shaped melt pools, a chessboard-like grain pattern and has a cube texture {100}<001>. Recrystallized grains were observed in the samples treated at 1150 °C for 15 min, as well as the samples treated for longer periods and at higher temperatures. Recrystallization was observed to start from high dislocation density regions, including the overlapping melt pools and the borders of the chessboard-like pattern. The initial cube texture transforms into a first-generation cube-twin texture {122}<212> via a twinning-assisted recrystallization mechanism. Then, those recrystallization nuclei sweep through the high defect density matrix; during which almost no new twins are formed. The samples treated at 1250 °C are almost completely recrystallized, which forms a weaker cube texture and a stronger P-orientation {011}<112>. However, the growth of recrystallized grains is very limited due to the presence of non-coherent precipitates.

* Corresponding author.
E-mail address: merve.dogu2@mail.dcu.ie (M.N. Doğu).

https://doi.org/10.1016/j.jmrt.2022.06.157

1. Introduction

Ni-based superalloys, the most extensively-developed superalloy family, have been widely used for aerospace and industrial applications over the past four decades for their outstanding high-temperature mechanical properties [1,2]. IN718, developed by the Nickel Corporation in the 1950s, possesses superior properties such as excellent oxidation and corrosion resistance, good weldability and high-temperature mechanical property stability up to 650 °C [3–5]. For this reason, IN718 is used in the aerospace industry (i.e. aircraft gas turbine disks, vanes, combustion chamber, rocket engine parts), chemical and petrochemical industries (i.e. bolts, valves, fans, tubing), nuclear power systems, marine architecture and pollution control equipment [6].

IN718 can have multiple phases shown in Table 1 depending on the elemental composition, heat-treatment conditions, and solidification. IN718 is a precipitation-strengthened Ni-based superalloy based on the austenite (γ) matrix. The primary strengthening phase is body-centered tetragonal (BCT) γ" (Ni_3Nb, $D0_{22}$) and the auxiliary strengthening phase is face-centered cubic (FCC) γ' ($Ni_3(Al, Ti)$, $L1_2$). These phases have a coherent or semi-coherent particle–matrix interface. The γ" (a coherent disc-like morphology with {100} habit plane) has higher coherency strain and antiphase boundary (APB) energy, so the strengthening effect of γ" is greater than γ' [7]. The metastable γ" can transform into the stable orthorhombic δ phase (Ni_3Nb, $D0_a$) over a long period of exposure to high temperatures (above 700 °C). δ phase, Laves (brittle intermetallic compound) and MC carbide have incoherent particle–matrix interfaces. However, these phases can be detrimental to the mechanical properties when they are extremely coarse and acicular. On the other hand, the δ phase can also lead to grain refinement. The mechanical properties can also be controlled by adjusting the size and distribution of the IN718 phases [4,8].

Conventional manufacturing techniques such as casting, wrought and powder metallurgy are used to produce IN718 and these methods provide reasonable mechanical properties. However, the machining of IN718 is difficult due to its low material removal rate and high shear strength. Additionally, many industries, particularly the aerospace industry, require highly complex geometries which are difficult to produce in a single production step with conventional manufacturing techniques [1,9]. For this reason, a more convenient manufacturing technique is necessary to produce IN718 geometries.

Additive manufacturing (AM) techniques provide significant advantages over conventional manufacturing techniques such as greater design freedom, near-net-shape fabrication, high material-use efficiency and alleviating the machining difficulty resulting from conventional manufacturing techniques [10,11]. The L-PBF process, also known as selective laser melting (SLM), is a metal AM technique that uses a focused laser beam to melt metal powder [12,13]. The production mechanism of the L-PBF process is based on layer-by-layer production according to the created CAD model and was explained in a detail in previous studies [14–17]. Furthermore, the L-PBF process possesses a low buy-to-fly ratio, enabling the manufacturing of complex geometries in a single production step and often provides cost and time-saving advantages over conventional manufacturing [8]. However, the high cooling rate of the L-PBF process causes rapid solidification leading to the formation of non-equilibrium phases such as Laves and carbides, inhibition of the precipitation strengthening phases, and microsegregation of the refractory elements such as Nb and Mo and residual stresses. These can decrease mechanical performance [18,19]. For this reason, post-heat treatments are often used as a common practice to dissolve detrimental phases (i.e. Laves), reduce possible residual stresses, and to optimize the microstructure and mechanical properties of the IN718 produced by the L-PBF [20].

Different post-heat treatments provide different microstructure and mechanical properties. These post-heat treatments can be categorized as solution heat treatment (SHT) improving mechanical properties by dissolving detrimental phases, stress-relieve heat treatment reducing residual stress and texture, aging (single or double) providing precipitation of strengthening phases, homogenization reorienting columnar grains and hot isostatic pressing (HIP) increasing density by decreasing defects [6]. Thus, optimization of the post-heat treatments is a significant step to obtain desired properties. Recently, the effects of heat treatments on IN718 produced with the L-PBF process have been investigated in several studies [3,8,18–24].

In the literature, solution heat treatment was generally performed with fast cooling (water quench or air cooling) for the IN718 produced by the L-PBF. Although a few studies [21,23–25] investigated solution heat treatment followed by furnace cooling (FC), a detailed investigation of the effects of FC during solution heat treatment on the IN718 produced by the L-PBF is necessary to fill a gap in the literature. Moreover, there are limited studies on the recrystallization and grain growth kinetics of L-PBF manufactured IN718. In this work, the influence of three different solution heat treatment

Table 1 – Phases in IN718 (adapted from [7,26]).

Phase	Crystal structure	Chemical formula	Solvus temperature (°C)
gamma (γ)	FCC	Ni	1227-1320 (solidus) 1260-1364 (liquidus)
gamma prime (γ′)	FCC (ordered $L1_2$)	$Ni_3(Al,Ti)$	850-970
gamma double-prime (γ")	BCT (ordered $D0_{22}$)	Ni_3Nb	910-940
delta (δ)	Orthorhombic (ordered $D0_a$)	Ni_3Nb	990-1020
Laves	Hexagonal (C_{14})	$(Ni, Cr, Fe)_2(Nb, Ti)$	1010-1160
metal carbide (MC)	Cubic (B_1)	(Nb, Ti)C	1260-1305

Table 2 – Chemical composition of the gas atomized IN718 powder, and ASTM F3055-14a standard [27].

Elements (wt.%)	Ni	Cr	Fe	Mo	Co	Al	Ta + Nb	Ti	C	Cu	Mn	Si	P	S	B
IN718 Powder	53.15	19.58	Balance	3.12	0.14	0.14	5.01	1.0	0.03	0.04	0.03	0.04	0.004	0.001	<0.01
ASTM F3055–14a	50–55	17.0–21.0	Balance	2.80–3.30	0–1	0.2–0.8	4.75–5.50	0.65–1.15	0–0.8	0–0.3	0–0.35	0–0.35	0–0.015	0–0.015	0–0.006

temperatures (1050, 1150 and 1250 °C) and holding times (15, 45 and 90 min) followed by FC under argon atmosphere on the recrystallization and grain growth behaviour of IN718 produced by the L-PBF was investigated. Microstructure and grain examination of the samples was performed using an optical microscope (OM), scanning electron microscope (SEM) and EBSD. Texture evolution of the samples was investigated using EBSD and microhardness values of the samples were measured by the Vickers microhardness test.

2. Materials and methods

2.1. *Raw materials and L-PBF process parameters*

Gas atomized IN718 powder with the particle size ranging from 10 to 45 μm was used for the L-PBF process. The chemical composition of the IN718 powder and the standard specification for Additive Manufacturing of Ni alloy (ASTM F3055-14a [27]) are given in Table 2. In this study, ten IN718 cubes ($10 \times 10 \times 10$ mm^3) were fabricated using SLM Solutions 280HL machine with the identical process parameters shown in Table 3. All of the IN718 cubes were produced in the z direction which is parallel to the build direction. Then, all IN718 cubes were removed from the build plate using wire-EDM prior to heat treatment.

2.2. *Heat treatments*

Before heat treatments, IN718 cubes were cleaned using acetone and ethanol, respectively. Then, the cleaned and dried IN718 cubes were placed into an atmosphere-controlled horizontal tube furnace (Lenton Tube Furnace 1500° LTF 16) at room temperature. After purging with high purity argon gas for 5 min, solution heat treatment was carried out under high purity argon gas flow at various temperature and holding time combinations. Subsequently, samples were cooled down to room temperature in the furnace under high purity argon gas (cooling rate of 5 °C/min). Table 4 shows the summary of the solution heat treatments applied for the IN718 cubes.

Table 3 – L-PBF process parameters for the IN718 cubes.

Process Parameters	Unit	Value
Layer thickness	μm	30
Preheating temperature	°C	200
Beam diameter	μm	85
Laser power	W	200
Laser speed	mm/s	945
Hatch distance	mm	0.12
Stripe length	mm	10
Starting angle	°	45
Rotation angle	°	90
Energy density	(J/mm^3)	59

Cubes were all fabricated using a (45, 90) scan pattern, which refers to a 45° laser starting scan angle with respect to the cube x-axis direction, and a 90° rotation angle per layer.

Table 4 – Summary of the solution heat treatments applied for IN718 cubes.

Description	Temperature (°C)	Holding time (min)
AB (as-built)	None	None
1050-15	1050	15
1050-45	1050	45
1050-90	1050	90
1150-15	1150	15
1150-45	1150	45
1150-90	1150	90
1250-15	1250	15
1250-45	1250	45
1250-90	1250	90

Furnace cooling (5 °C/min) under argon atmosphere.

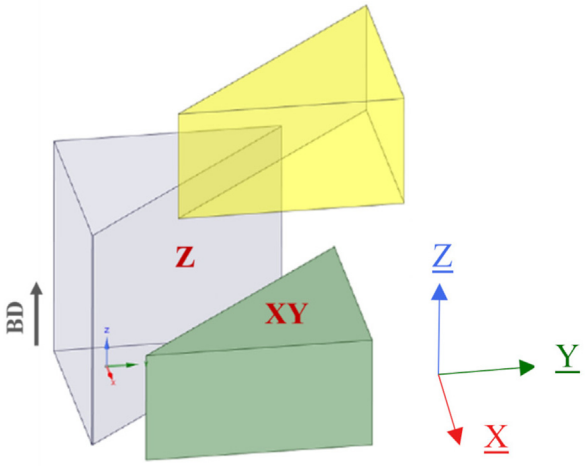

Fig. 1 – Schematic of Z and XY examination planes cut from the IN718 cubes (BD: build direction).

2.3. *Materials characterization*

For the metallographic examination, IN718 cubes were cut as shown in Fig. 1 to examine both Z (parallel to the build direction) and XY (perpendicular to the build direction) planes. After that, the samples were mechanically ground using conventional SiC grinding papers up to 1200 grit size, then polished with progressively finer diamond suspensions (9, 3, 1 μm). The etching step was a challenge for this study. Different etchants such as Waterless Kalling's were tried on the samples. However, the Glyceregia reagent (15 ml HCl, 10 ml glycerol and 5 ml HNO_3) provided the best result [28]. Although generally swabbing is recommended for the Glyceregia reagent, it caused scratches for the solution heat-treated samples. Also, the immersion method provided heterogeneous etched surfaces. Therefore, the etchant was dropped on the samples using a pipette to obtain homogeneously etched surfaces. Microstructures of the AB and solution heat-treated samples were examined by OM (Nikon Eclipse LV150) and SEM (ZEISS Merlin Scanning Electron Microscope). Additionally, EBSD analysis was carried out in the ZEISS Merlin SEM using an acceleration voltage of 15 kV and 6.0 nA probe current. In addition to the above polishing steps, an additional final polishing step was applied using 0.25 μm fumed silica (OP–S) was applied before the EBSD analysis. The mapping areas of 500 μm × 500 μm were indexed with a step size of 1 μm. EBSD raw data was post-processed using TSL OIM Analysis™ software. Points with CI (confidence index) below 0.1 were removed and twin boundaries were excluded for grain size calculations. The Vickers microhardness tests were carried out for both Z and XY planes from 15 points for each plane using Zwick/Roell Zhu microhardness tester 2.5 with a load of 1 kg according to ASTM 384-17 [25].

3. Results

3.1. *Microstructure and hardness in the AB condition*

Fig. 2 shows the microstructure of the AB sample. Optical micrographs of the Z and XY planes are shown in Fig. 2(a, b), respectively. Similar to other studies [15,21,29,30], bowl-shaped melt pools (Z plane) resulting from the Gaussian energy distribution of the laser beam and laser scanning paths line by line (XY plane) were observed in the AB sample. The columnar dendritic microstructure, the columnar grains with cellular structure and very fine dendrites are the typical microstructure of IN718 produced by the L-PBF and the melt pool boundary indicated with a white dashed line are displayed in Fig. 2(c). The magnified SEM images exhibit columnar and cellular substructures with an average spacing of 477 ± 171 nm and 581 ± 125 nm, respectively. Additionally, the brittle Laves phase which should be dissolved with solution heat treatment and γ matrix can be observed in the magnified SEM images indicated by red arrows. Although the overall heat flow direction is almost parallel to the building direction, the columnar dendrites have different grain growth directions resulting from complicated temperature fields in the melt pool [15].

The grain morphologies of the Z and XY planes can be clearly seen in the inverse pole figure (IPF) maps displayed in Fig. 2(d, e) and image quality and grain boundaries (IQ & GBs) maps shown in Fig. 2(f, g). The Z plane contains mainly elongated grains which are parallel to the build direction. On the other hand, the XY plane contains a chessboard-like grain pattern due to the scanning strategy (45° starting angle with 90° rotation angle between layers). Additionally, the area-weighted average grain size values were obtained from EBSD and the grain size values are 24.2 ± 5.8 μm and 13.3 ± 3.9 μm which are similar to those reported in the literature [31,32] for the Z and XY planes, respectively (Table 5 and Fig. 3(a)).

The kernel average misorientation (KAM) maps of the Z and XY planes are displayed in Fig. 2(h) and (i), respectively. KAM can be defined as the measure of the local grain misorientation and the KAM map displays the average misorientation of each pixel with respect to its neighbours. In general, high KAM values represent high plastic strain and dislocation density [33,34]. The KAM maps are labelled with a rainbow scale; where blue and red represent the minimum and maximum misorientation (0-5°), respectively. The overlapping regions have a higher KAM value compared to inside of the melt pools shown in Fig. 2(h) and the KAM value of the Z

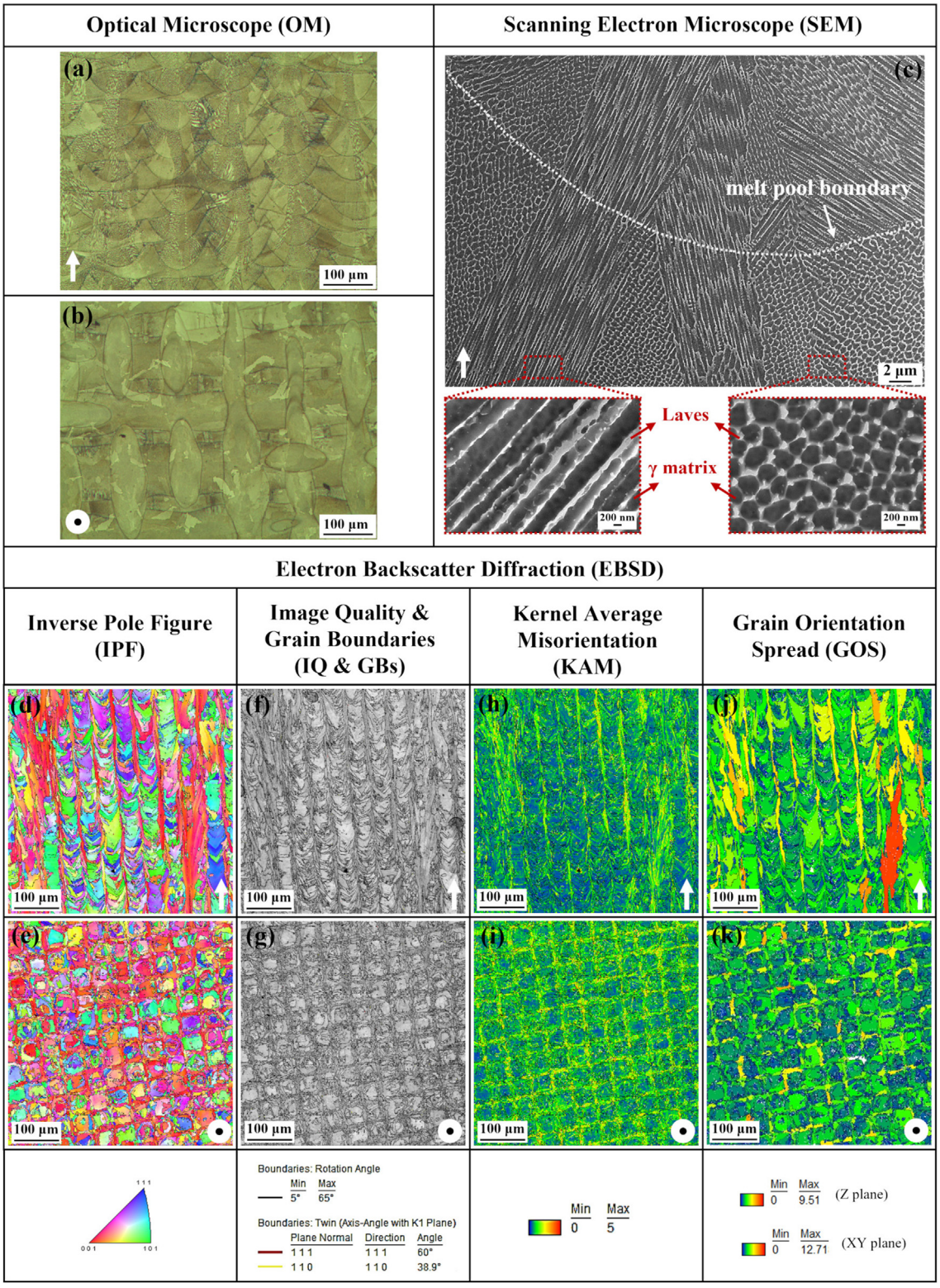

Fig. 2 – (a–b) Optical micrographs, (c) SEM image, (d–e) IPF maps, (f–g) IQ and GBs maps, (h–i) KAM maps and (j–k) GOS maps of the AB sample. Z plane (parallel to build direction) and XY planes (perpendicular to build direction) are indicated with an arrow and a dot, respectively.

plane is 0.99° (Table 6). Furthermore, the KAM value of the XY plane is 1.19° shown in Table 6 and the borders have a higher KAM value compared to the center of the chessboard-like pattern as shown in Fig. 2(i). This finding is consistent with the study of Aota et al. [35] who reported that the coarse grains are located at the center of the chessboard-like pattern having

Table 5 – The average hardness and grain size values of the AB and solution heat-treated samples.

Sample	Hardness (HV1)		Average grain size (μm)	
	Z plane	XY plane	Z plane	XY plane
AB	327.1 ± 4.6	323.5 ± 7.4	24.2 ± 5.8	13.3 ± 3.9
1050-15	394.9 ± 4.9	400.3 ± 7.2	20.5 ± 5.7	13.1 ± 3.8
1050-45	399.8 ± 6.2	399.8 ± 7.8	19.5 ± 5.7	14.5 ± 4.1
1050-90	397.2 ± 6.3	395 ± 4.3	21.1 ± 5.8	13.4 ± 3.9
1150-15	401.6 ± 3.3	398.4 ± 5.3	21.6 ± 6.2	14.1 ± 4.1
1150-45	414.1 ± 6.5	414.9 ± 6.2	46.2 ± 10.0	41.3 ± 9.4
1150-90	411.7 ± 8.4	417.1 ± 7.5	35.8 ± 9.0	39.8 ± 9.5
1250-15	415.7 ± 4.4	426.3 ± 6.2	45.9 ± 13.3	60.1 ± 19.8
1250-45	414.7 ± 5.4	420.3 ± 8.2	50.8 ± 14.6	63.4 ± 21.4
1250-90	409.4 ± 6.2	418.4 ± 6.0	58.7 ± 18.1	63.2 ± 19.7

a lower KAM value and the borders of the chessboard-like pattern contain the fine grains having a higher KAM value. Additionally, the number fraction versus the KAM graph is shown in Fig. 3(b).

The high cooling rate during solidification causes local strain inhomogeneity and accordingly a high dislocation density. The internal plastic strain gradients cause the geometrically necessary dislocations (GND). Thus, a high GND density indicates high plastic strain gradients [35]. Fig. 3(c) shows the number fraction versus the GND density graph. The average GND densities of the Z and XY planes are 28.61 and 36.33 shown in Table 6, respectively. The grain orientation spread (GOS) can be defined as the average of the misorientation angles to the grain mean orientation [33]. The GOS maps labelled with a rainbow scale and blue and red colours show minimum and maximum GOS angles. A similar trend with the KAM was observed for the GOS of Z and XY planes. The columnar grain regions have a higher GOS value compared to inside of the melt pools shown in Fig. 2(j) and the borders have a higher GOS value compared to the center of the chessboard-like pattern as shown in Fig. 2(k). The correlated number fraction versus misorientation angle graph is displayed in Fig. 3(d). The yellow line shows the Mackenzie distribution for randomly oriented cubic polycrystals. The misorientation distribution of the AB sample shows the predominance of low angle grain boundaries (<10°) having more substructure and dislocation density [36].

The hardness values of the Z and XY planes were measured as 327.1 ± 4.6 HV and 323.5 ± 7.4 HV respectively (see Table 5). Similar hardness values were reported in the review article of Sanchez et al. [6].

3.2. *Microstructure and hardness in the solution heat-treated condition*

The applied solution heat treatments in this study are displayed in Table 4. Optical micrographs of the solution heat-treated samples in different conditions show the microstructural evolution according to the solution heat treatment temperature and holding time (Fig. 4). There is no significant difference among the microstructures of the 1050-15, 1050-45, 1050-90 and 1150-15 samples and the bowl-shaped melt pools

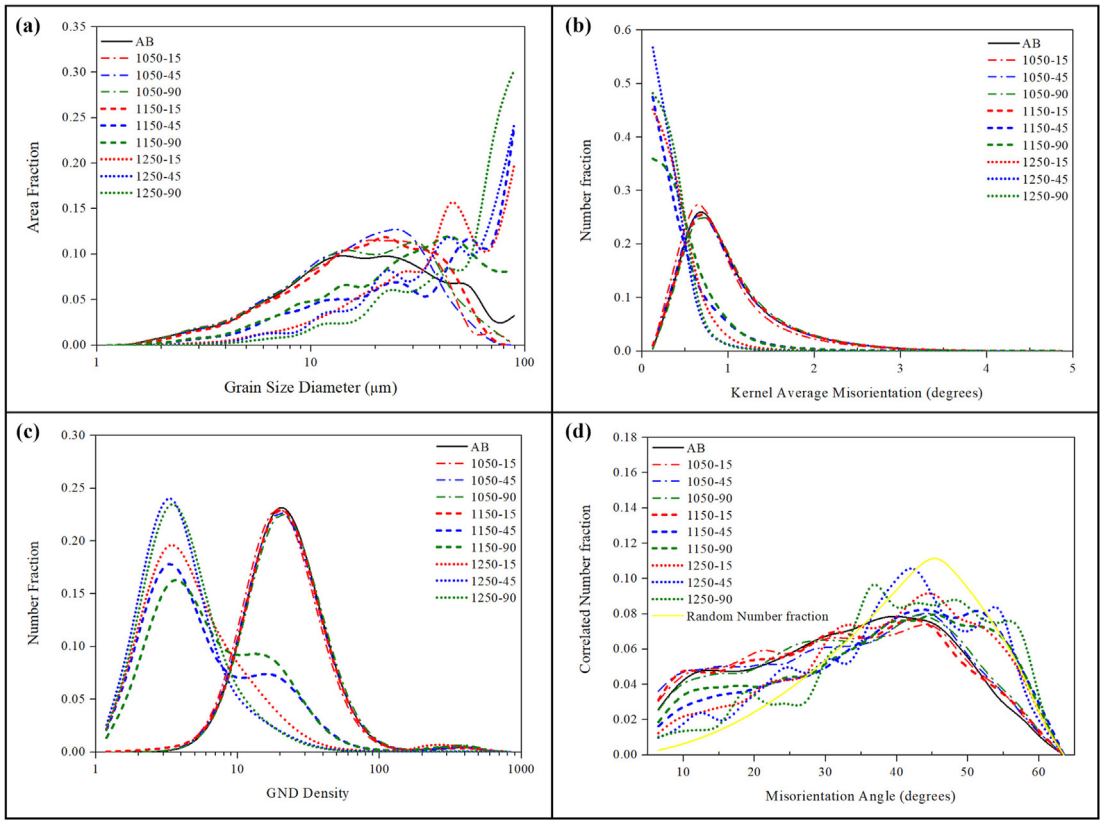

Fig. 3 – (a) Grain size, (b) KAM, (c) GND density and (d) misorientation angle distributions of the AB and solution heat-treated samples.

Table 6 – The kernel average misorientation (KAM), geometrically necessary dislocation density (GND), recrystallization fraction values of the AB and solution heat-treated samples.

Sample	KAM (°)		GND density		Recrystallization Fraction
	Z plane	XY plane	Z plane	XY plane	
AB	0.99 ± 0.58	1.19 ± 0.66	28.61	36.34	0.24
1050-15	0.93 ± 0.58	1.16 ± 0.66	27.74	34.66	0.31
1050-45	0.99 ± 0.58	1.12 ± 0.64	29.15	34.07	0.34
1050-90	1.02 ± 0.58	1.15 ± 0.63	31.22	35.21	0.42
1150-15	0.98 ± 0.56	1.08 ± 0.62	28.15	31.53	0.31
1150-45	0.42 ± 0.38	0.40 ± 0.37	13.10	11.05	0.76
1150-90	0.45 ± 0.36	0.41 ± 0.37	14.60	11.15	0.82
1250-15	0.35 ± 0.28	0.26 ± 0.21	11.81	6.53	0.90
1250-45	0.28 ± 0.20	0.29 ± 0.20	5.33	6.67	0.92
1250-90	0.30 ± 0.19	0.27 ± 0.16	6.05	5.97	0.96

and scanning paths are still visible (Fig. 4(a-d)). The first recrystallized grains indicated by the red dashed lines were observed in the 1150-15 sample (Fig. 4(d)). Therefore, 1150 °C for 15 min can be accepted as starting of the recrystallization in this study. On the other hand, there is a significant difference in the microstructure of the 1150-45 sample compared to the previous samples and twin boundaries with the recrystallized grains can be clearly seen in Fig. 4(e). For this reason, the recrystallization start temperature can be accepted as 1150 °C for IN718 produced by the L-PBF in this study. Additionally, the area-weighted average grain size values are similar up to 1150-15 sample; however, two times increment in grain size was observed for the 1150-45 sample having 46.2 ± 10 μm and 41.3 ± 9.4 μm area-weighted average grain size values for the Z and XY planes, respectively (see Table 5 and Fig. 3(a)). Furthermore, the grain growth followed the trend of increased recrystallization with the solution heat treatment temperature increment (see Fig. 4(f-i) and Table 5).

Fig. 5 shows the SEM images of the 1050-45, 1150-15, 1150-45 and 1250-45 samples. All of the samples have precipitates which can be MC carbide, δ phase (needle-like precipitates at the grain boundaries) and Laves at the grain boundaries (Fig. 5(a-d)). Additionally, the high magnified SEM images indicated by red dashed lines display the strengthening precipitate phases (γ" and γ′) which precipitate during the slow cooling. However, transmission electron microscopy (TEM) is required to better understand how the precipitated phases formed according to the solution temperature and time.

EBSD maps of the Z and XY planes of 1050-45, 1150-15, 1150-45 and 1250-45 samples are shown in Figs. 6 and 7, respectively. As it was observed in the optical micrographs (Fig. 4), the grain morphologies of the 1050-45 and 1150-15 samples are similar for both Z and XY planes and it can be seen in both IPF maps (Fig. 6(a, b)) as well as IQ & GBs maps (Fig. 7(a, b)). On the other hand, the microstructural change in the 1150-45 sample, along with the mostly recrystallized grains also mentioned above section can be clearly seen in Figs. 6(c) and 7(c) for both Z and XY planes. Twin boundaries indicated by the red lines in IQ & GBs maps were firstly observed in the 1150-45 sample (Figs. 6(c) and 7(c)). Twin

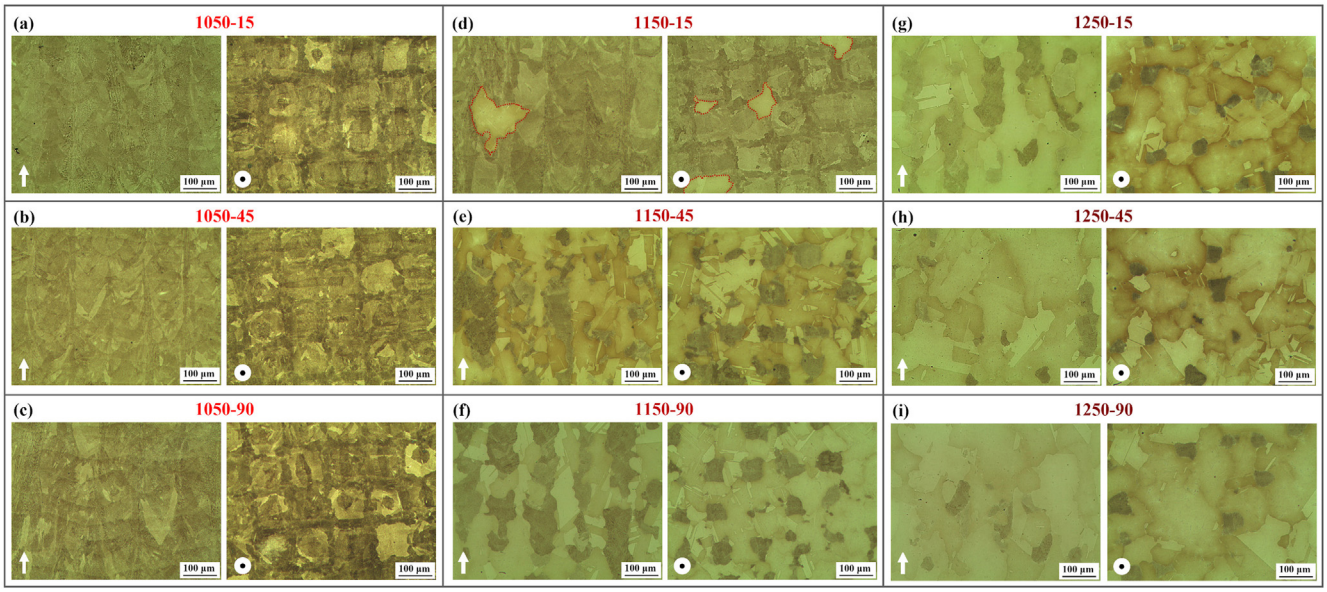

Fig. 4 – Optical micrographs of the solution heat-treatment conditions, (a) 1050 °C for 15 min, (b) 1050 °C for 45 min, (c) 1050 °C for 90 min, (d) 1150 °C for 15 min, (e) 1150 °C for 45 min, (f) 1150 °C for 90 min, (g) 1250 °C for 15 min, (h) 1250 °C for 45 min and (i) 1250 °C for 90 min. Z plane and XY plane are shown with an arrow and a dot, respectively.

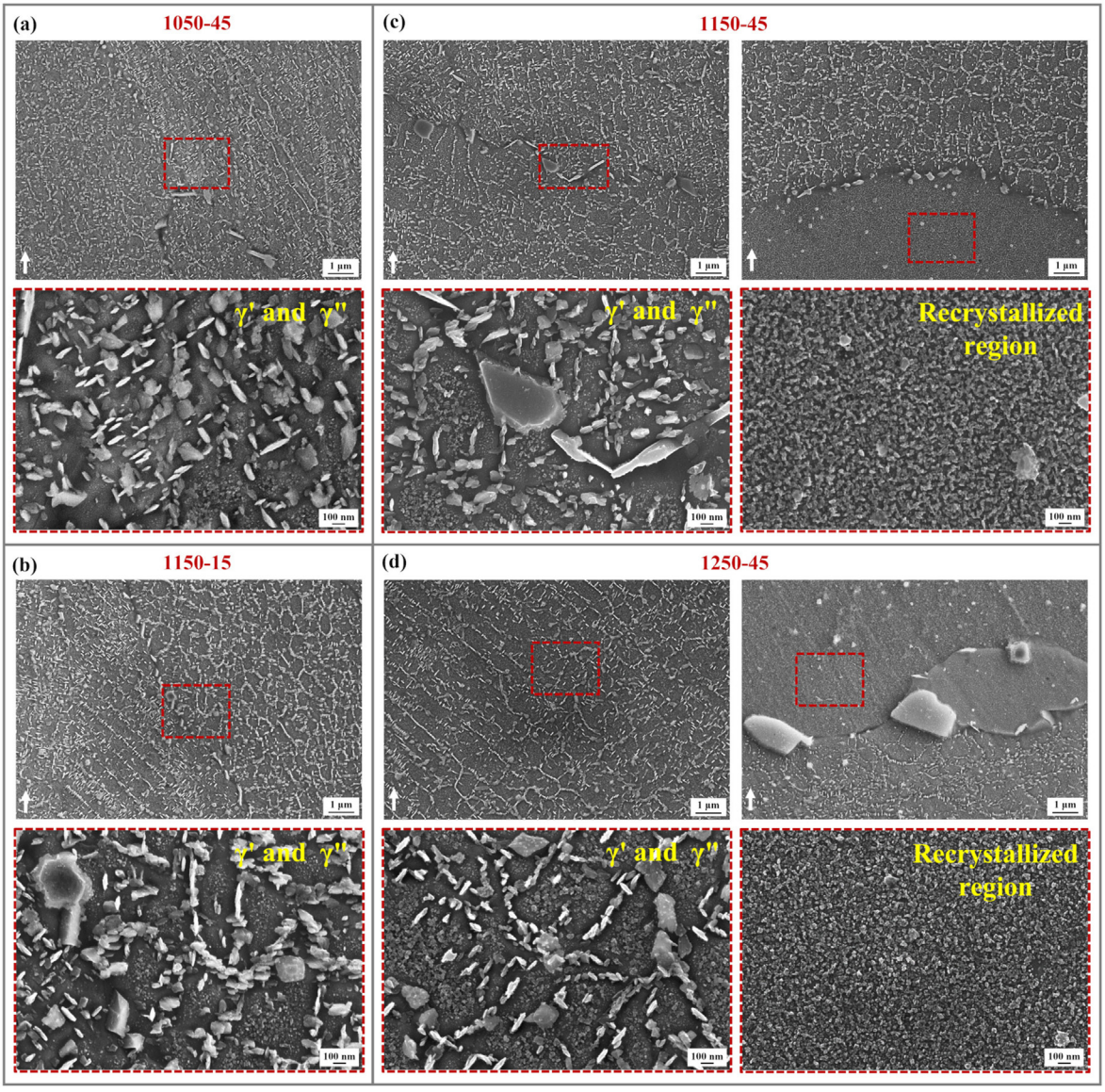

Fig. 5 – SEM images of the solution heat-treated samples at (a) 1050 °C for 45 min, (b) 1150 °C for 15 min, (c) 1150 °C for 45 min and (d) 1250 °C for 45 min; the red dashed lines represent first recrystallized grains.

boundaries can be called as coherent twin boundaries (Σ3) and twin-related grain boundaries (Σ9 and Σ27), are special boundaries and they can contribute to the material strength and resistance to intergranular degradation [37,38]. The twin boundary fractions are 0.366 (at 60° on (111)) and 0.026 (at 38.9° on (110)) for the Z plane and 0.377 (at 60° on (111)) and 0.023 (at 38.9° on (110)) for the XY plane. Moreover, twin boundaries are also visible in the optical micrographs (Fig. 4(e)). Additionally, the twin boundaries were observed in the 1250-45 sample (Figs. 4(h), 6(d) and 7(d)). The twin boundary fractions are 0.509 (at 60° on (111)) and 0.026 (at 38.9° on (110)) for the Z plane and 0.503 (at 60° on (111)) and 0.026 (at 38.9° on (110)) for the XY plane. It can be said that the twin boundary fraction increased with the increment of solution heat treatment temperature.

As it was explained in section 3.1., the overlapping regions and the borders of the chessboard-like pattern have a higher KAM value due to the higher dislocation density [35]. There is no significant difference in the AB, 1050-45 and 1150-15 samples in terms of the KAM values shown in Table 6 and Fig. 3(b). However, there is about 57% decrease in the KAM value of the 1150-45 sample (Table 6 and Fig. 3(b)) due to the recrystallization. The blue regions which are on the KAM maps of the 1150-45 sample (Figs. 6(c) and 7(c)) can be called as recrystallized grains. Additionally, as it was expected, the KAM value decreased with the increment of solution heat treatment temperature (Table 6 and Fig. 3(b)). Furthermore, the 1250-45 sample has more recrystallized grains compared to the 1150-45 sample (Figs. 6(d) and 7(d)). On the other hand, the average GND density values (Table 6) reduced with the recrystallization. The 1150-45 sample has about 54% less GND density and the 1250-45 sample has about 81% less GND density compared to the AB, 1050-45 and 1150-15 samples. Moreover, the

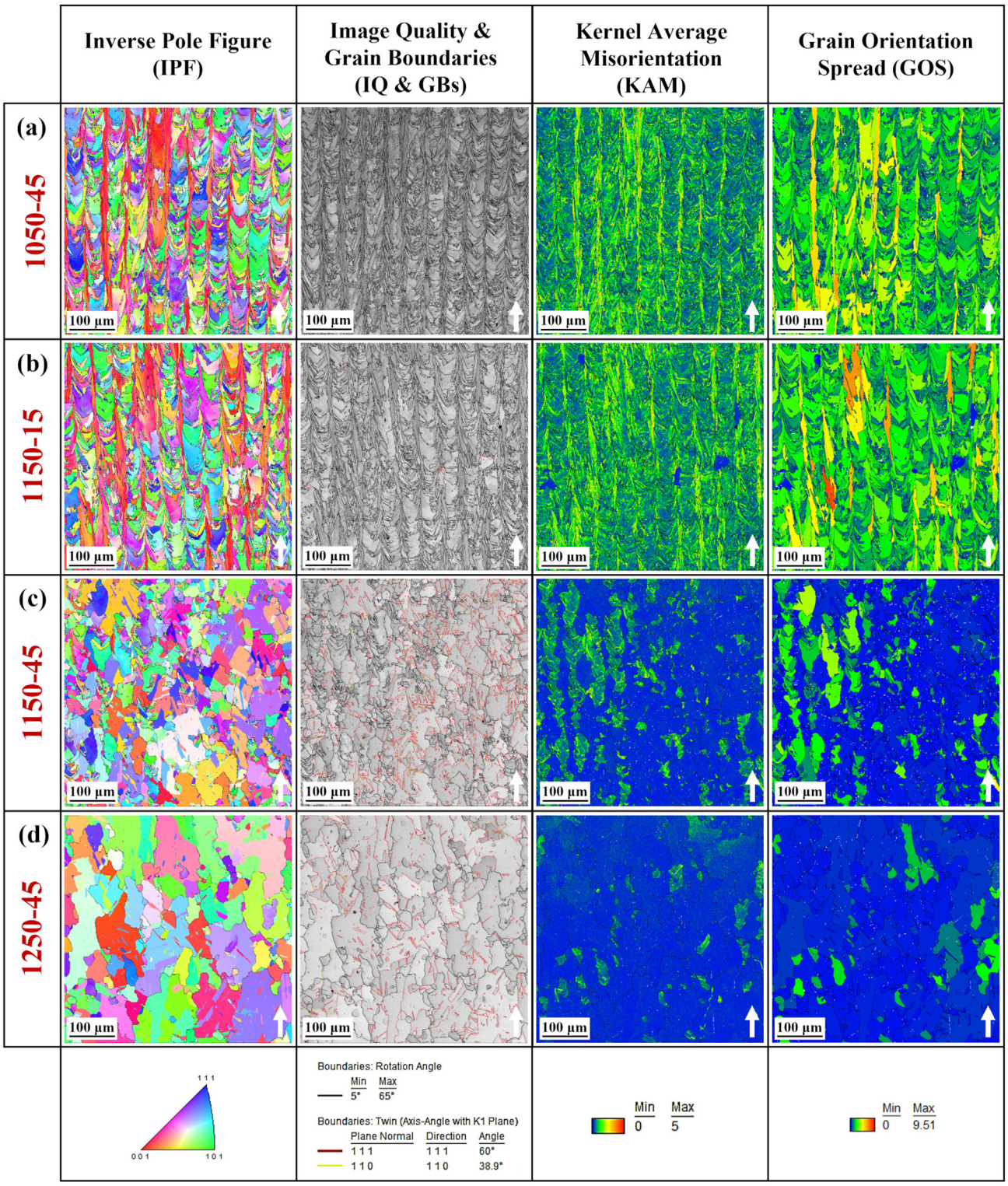

Fig. 6 – EBSD maps of the solution heat-treated samples; (a) 1050-45, (b) 1150-15, (c) 1150-45 and (d) 1250-45. Z plane (parallel to build direction) is indicated with an arrow.

recrystallization and grain growth can be seen in the GOS maps shown in Fig. 6(a-d) and 7(a-d) for the 1150-45 and 1250-45 samples. Additionally, the misorientation angle graphs of the 1150-45 and 1250-45 samples (Fig. 3(d)) approach to the Mackenzie distribution and also there is a second peak at 60° for the 1150-45 and 1250-45 samples.

The hardness values of the Z and XY planes of the samples are given in Table 5. In contrast to the AB sample, higher hardness values were obtained in the solution heat-treated samples due to precipitated phases during the slow cooling. Moreover, there was no significant difference in the hardness values of the Z and XY planes of the samples. The 1150-45 and

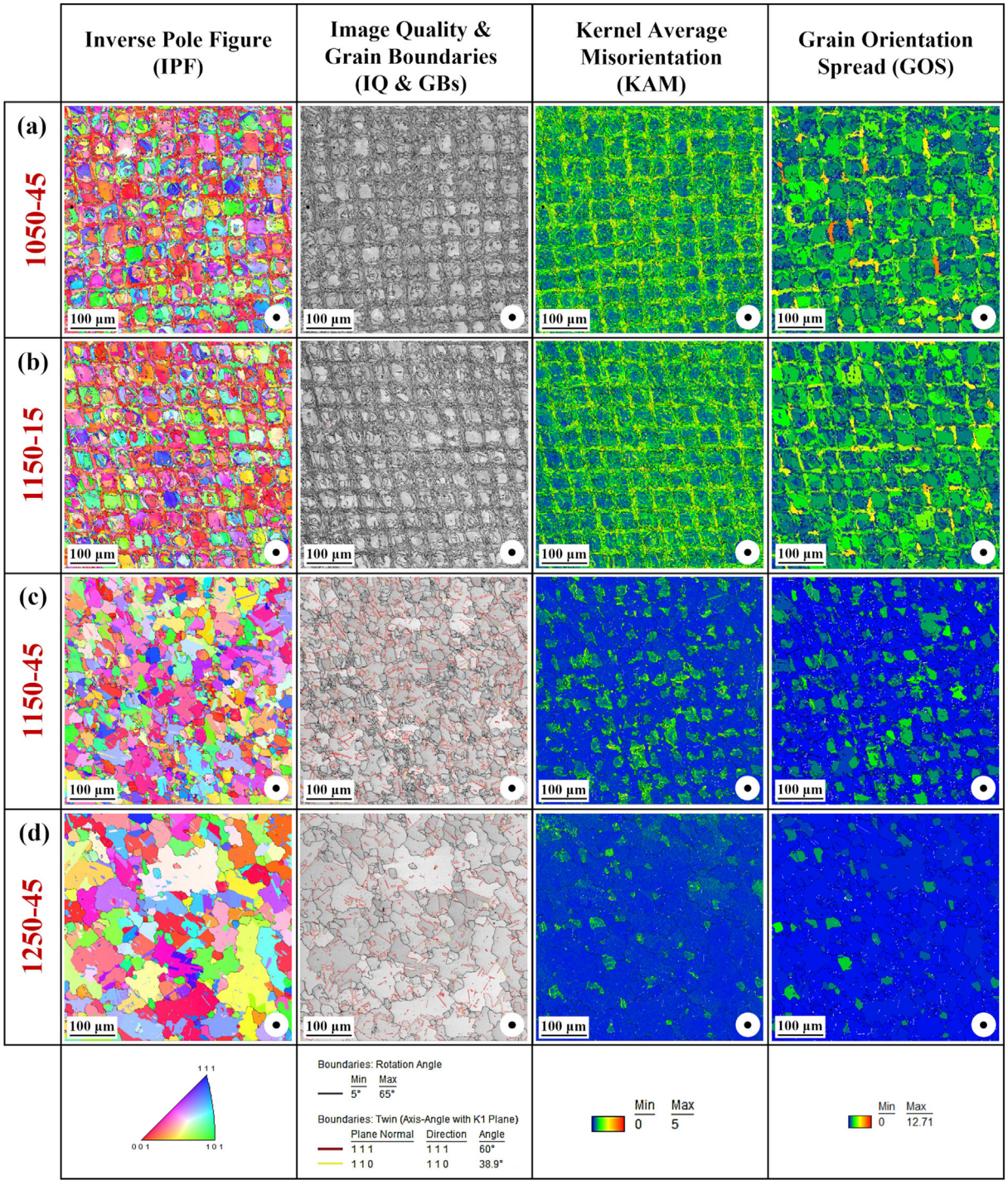

Fig. 7 – EBSD maps of the solution heat-treated samples; (a) 1050-45, (b) 1150-15, (c) 1150-45 and (d) 1250-45. XY plane (perpendicular to build direction) is indicated with a dot.

1250-45 samples have higher hardness values (around 414 HV for the Z plane) than the 1050-45 and 1150-15 samples.

3.3. *Texture in the AB and solution heat-treated conditions*

The texture of the samples was examined by using the EBSD technique. Fig. 8 shows the PF and IPF maps, only the corresponding {001} PF and [001] IPF were represented, of the AB, 1050-45, 1150-15, 1150-45 and 1250-45 samples. The maps belong to the Z plane which is parallel to the BD (build direction) of the samples. During the solidification from the liquid phase to the solid phase, the atoms prefer to move to the less close-packed planes and the grain growth direction occurs along <100> for FCC metals. For this reason, the typical solidification texture is well known as <100>//BD for the cubic materials because the grain growth occurs faster for the grains which have the <100> directions//the temperature gradient

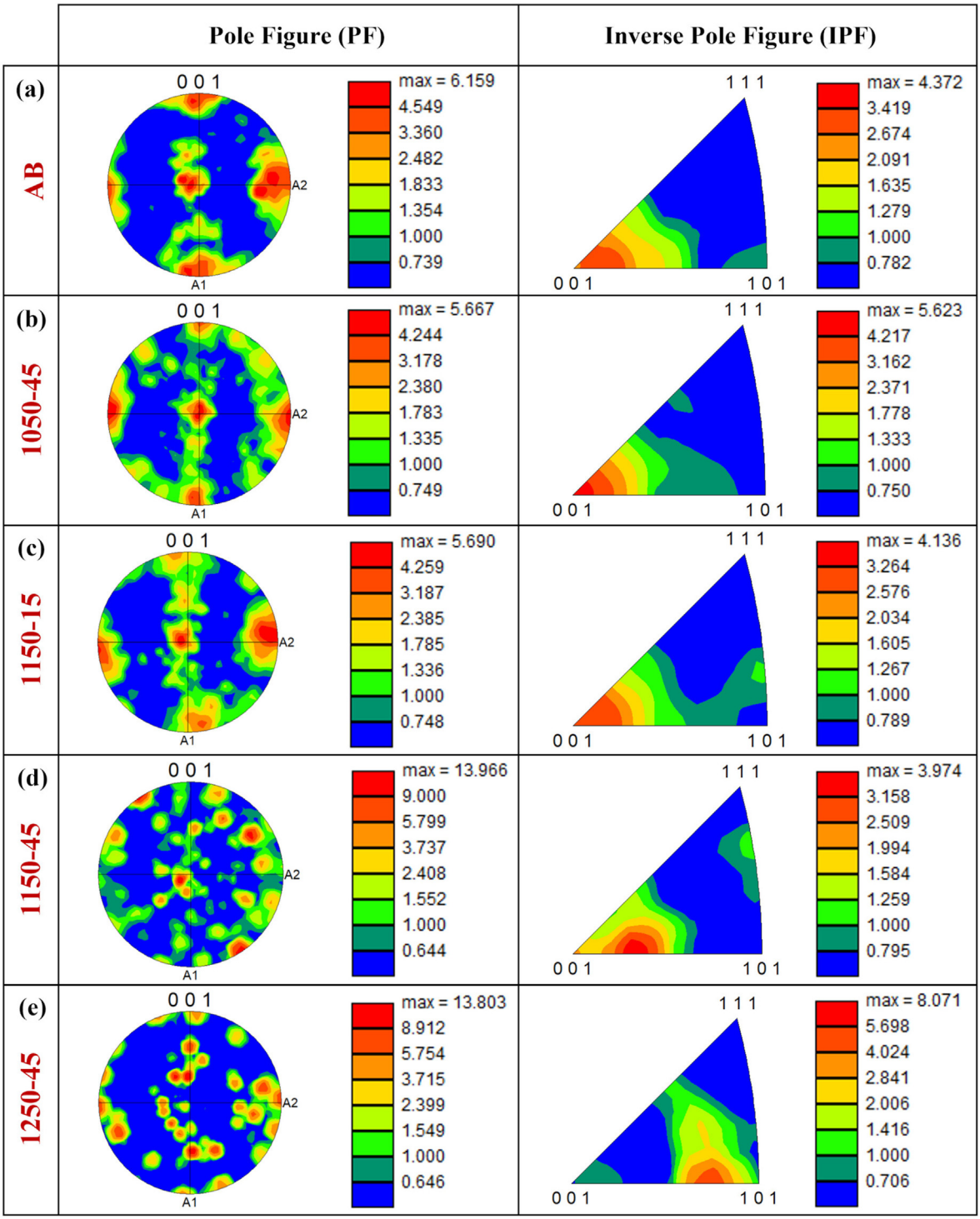

Fig. 8 – Pole figure (PF) and inverse pole figure (IPF) maps with respect to build direction of (a) AB, (b) 1050-45, (c) 1150-15, (d) 1150-45 and (e) 1250-45 samples.

during the solidification. Moreover, the typical cube texture is represented as {001}//<100> [33].

The texture was observed in the middle and four edges of the {001} PF map of the AB sample with the maximum intensity value of 6.159 (Fig. 8(a)) and this texture is a typical example for the cube texture. Moreover, the IPF map of the AB sample shows the <001>//BD texture component with the maximum intensity value of 4.372. It can be said that the AB sample has the {001}//<001> cube texture.

The PF and IPF maps of the 1050-45 and 1150-15 samples are shown in Fig. 8(b, c). When we compare the PF and IPF maps of these samples with the AB sample, there is no significant difference except similar intensity value differences and these samples also have the {001}//<001> Cube texture.

Indeed, it was expected for these samples because there was no significant difference in the microstructure, grain size, KAM, GND density and misorientation angle compared to the AB sample. On the other hand, the texture of the 1150-45 sample changed compared to the previous samples (Fig. 8(d)). This sample exhibits first generation cube twin texture {122}<212>. The 1250-45 sample shows a weaker cube texture and a more intense P-orientation {011}<122>.

4. Discussions

4.1. Microstructural and texture evolution of the AB sample

The growth process of the sub-structures during the L-PBF process was well explained in the study of Li et al. [19]. The nature of the L-PBF process provides rapid cooling and non-equilibrium solidification. The solidification microstructure is affected by the solidification rate (R), undercooling (ΔT), and temperature gradient (G), along with the process parameters of L-PBF. The structure size and morphology of solidification microstructure (planar, cellular, equiaxed dendritic, or columnar dendritic) are determined by GR and G/R, respectively. For example, the low cooling rates provide coarser structures (GR), whereas the finer structures can be obtained by increasing the cooling rate (GR). On the other hand, reducing the G/R ratio can give the planar, cellular, equiaxed dendritic, or columnar dendritic solidification microstructure [13,25,39]. The columnar dendritic and cellular microstructure was observed in this study (Fig. 2(c)).

The solidification sequence of IN718 is well established as follows: Liquid $\rightarrow \gamma \rightarrow \gamma + MC \rightarrow \gamma + MC + Laves$ [40]. The segregation of Nb in the inter-dendritic regions is inevitable due to its partitioning behaviour during the solidification of IN718. Deng et al. [29] reported that the cooling rate affects the segregation of Nb and the size of Laves phase, which can be significantly minimized by increasing the cooling rate. Indeed, the low amount and size of Nb precipitates can be obtained with the L-PBF process compared to casting due to rapid cooling [4]. According to the study of Tucho et al. [3], Laves phase, NbC and TiC can be observed in the sub-grain boundaries of the as-printed IN718. Although the main reason for these precipitates is the microsegregation Nb, Mo and Ti also segregate during the solidification. Additionally, Laves phase requires at least 10 wt.% Nb to form and it is well known that most of the segregated Nb are consumed by Laves phase [20]. In our study, Laves phase is clear in the AB sample (Fig. 2 (c)). Moreover, Laves is a brittle intermetallic phase and degrades the high-temperature tensile properties [8].

The combined effects of both the maximum heat flow directions and the alignment of easy grain growth directions at the melt pool boundaries determine the texture [30]. The preferred grain growth direction is < 100> along the heat-flow direction for the FCC crystal structure because atoms can move faster to the less close-packed planes [33]. The heat flow direction and the balance between G and R can be locally changed by altering the process parameters of the L-PBF (i.e., scanning strategy and energy density). Thus, the texture and microstructure can be modified [31]. Moreover, The cube texture {001}//<100> also observed in our study (Fig. 8(a)) was reported in the studies on IN718 produced by the L-PBF [6,30,31,41]. Additionally, when the heat flow direction is not parallel to the BD, weak <100>//BD and <110>//BD textures also can be observed in the FCC crystal structure [30]. Gokcekaya et al. [31] reported the unique crystallographic texture formation for IN718 produced by the L-PBF with a bidirectional scanning strategy. According to their study, a crystallographic lamellar microstructure (composed of <110>//BD-oriented main grains and <100>//BD-oriented sub-grains), a <110>//BD-oriented single crystal-like microstructure, and polycrystalline microstructure were obtained by changing the scan speed and laser power.

4.2. Microstructural and texture evolution of the solution heat-treated samples

The effects of the solution heat treatment temperature and holding time on IN718 produced by the L-PBF were given in section 3. There is no significant difference in the optical micrographs of 1050-15, 1050-45, 1050-90 and 1150-15 samples compared to the AB sample (Fig. 4(a-c)) in terms of microstructure. Also, the area-weighted average grain size, KAM and GND density values of these samples are close to the AB sample. Although the microstructure of the 1150-15 sample is similar to the AB sample, the first recrystallized grains were observed in the 1150-15 sample (Fig. 4(d)). Tucho et al. [3] reported 1100 °C as recrystallization start temperature which is reasonably consistent with the recrystallization start temperature found in this work (1150 °C). Moreover, recrystallization fraction and grain size diameter versus time graphs and also twin density versus grain size diameter graphs are shown in Fig. 9(a, b).

On the other hand, a significant microstructural difference was observed in the 1150-45 sample compared to the previous samples. Recrystallization was observed in the 1150-45 sample, although it was not completed. Additionally, twins which are a sign of recrystallization, along with 87.3% grain size increment were observed in the 1150-45 sample. As it was discussed before, the overlapping regions and the borders of the chessboard-like pattern have a higher KAM value due to the higher dislocation density. Therefore, the first recrystallized grains should be the grains that are in the overlapping regions and the boards of the chessboard-like pattern. This was clearly observed in the KAM map of the XY plane of the 1150-45 sample (Fig. 7(c)) and the blue regions are strain-free recrystallized grains. Furthermore, the GND density reduced 54% in the 1150-45 sample due to recrystallization. When we looked at the 1250-45 sample, near-complete recrystallization (92%) with the grain coarsening was observed. The grain size increment is around 118% compared to the AB sample. Most of the grains are strain-free recrystallized grains (Figs. 6(d) and 7(d)) and the average GND density reduced 81% in the 1250-45 sample compared to the AB sample. The coarsened grains in the 1150-45 and 1250-45 samples can be seen in the GOS maps (Figs. 6(c, d) and 7(c, d)). Moreover, there is a 39% increment of the twin boundary fraction compared to the 1150-45 sample. Jin et al. [42] reported that the density of annealing twins is inversely proportional to the grain size. Fig. 9(c) shows the twin boundary length per 500 × 500-micron

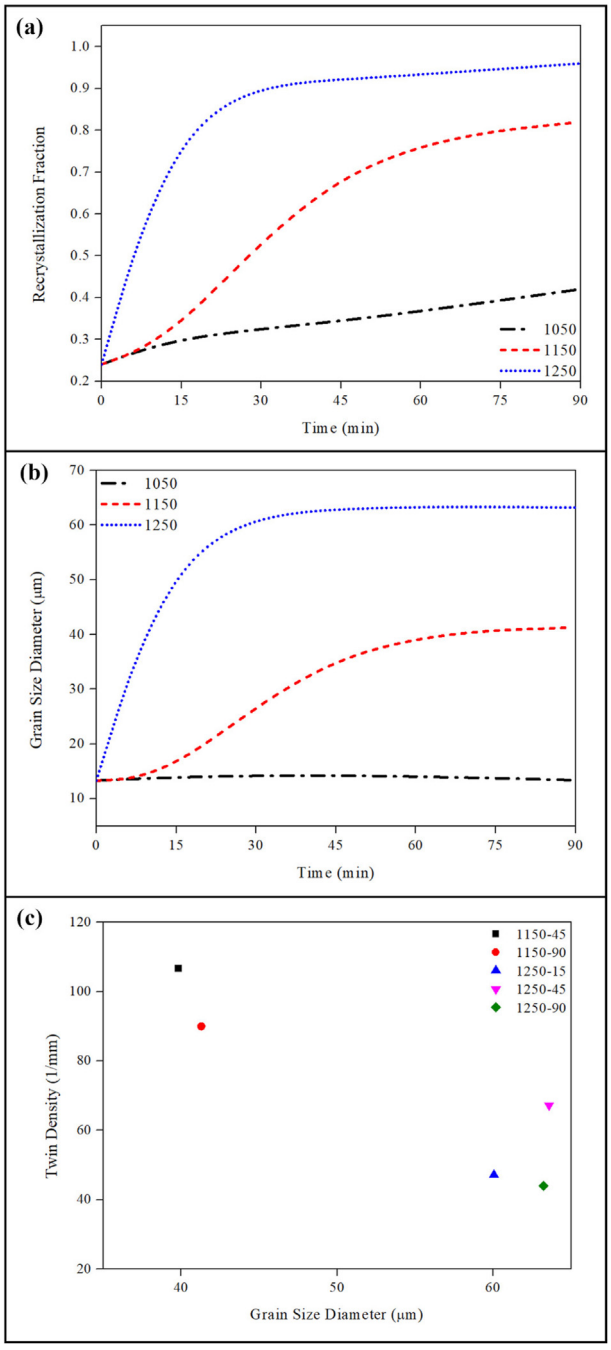

Fig. 9 – (a) Recrystallization fraction versus time, (b) grain size diameter versus time and (c) twin density versus grain size diameter graphs.

square area versus grain size graph. The misorientation angle of 60° (observed in the 1150-45 and 1250-45 samples) corresponds to one of coincident site lattice (CSL) type of boundaries, namely the Σ3, which can also be identified as coherent twin boundary. The results shown at Fig. 9 (c) agrees well with this study [40]. Both studies indicate that, almost no new twins are formed during grain growth. Moreover, as seen in Fig. 6(c) (IQ & GBs maps), the twins are mostly located at the grain edges next to non-recrystallized regions, rather than grain interiors. The same behaviour is observed in recrystallization of additively manufactured AISI 316 stainless steel samples reported by Aota et al. [35]. This behaviour was attributed to growth accident model, at which stacking faults are formed along a moving boundary, resulting in two different twin boundaries. One of them is an immobile, coherent twin boundary which is left behind, and the other is less coherent and highly mobile boundary that consumes the high defect density matrix [43–45].

There is a significant difference between the AB sample and solution heat-treated samples in terms of phases shown in SEM images (Fig. 2(c) and Fig. 5) and the FC (5 °C/min) can be shown as a reason for this difference. The precipitated phases were observed at both matrix and grain boundaries of the solution heat-treated samples (Fig. 5). The precipitation of γ" and γ′ strengthening phases is possible in the range of 600–900 °C during double aging treatment [19]. During FC, the cooling from 900 °C to 600 °C took 60 min which is enough time for the precipitation of γ" and γ′ strengthening phases [21]. In this study, the disk-like precipitates which are in the matrix of the solution heat-treated samples can be γ" shown in high magnified SEM images, which is consistent with the study of Huang et al. [21]. The slow cooling may cause the precipitation of δ phase, brittle Laves and the strengthening phases (γ" and γ′) according to the TTT [46] and CCT [25] curves. Moreover, at least 6–8 wt.% Nb is required for the δ phase and the metastable γ" can transform into a stable δ phase at temperatures between 700 and 1010 °C [3,25,47]. Generally, the δ phase which precipitates at the grain boundaries during heat treatment is considered an undesirable phase due to the adverse effects on the fracture toughness and ductility. On the other hand, it can be beneficial due to the increment stress rupture resistance and grain stabilization effects. The needle-like δ phase which inhibits micro-cracks and granular-shaped δ phase which acts as a pin between grain boundaries can be seen in the literature [48]. In this study, the needle-like δ phase was observed at the grain boundaries of the solution heat-treated samples. The local stress concentration, dislocation pile-up and premature failure can be due to too much δ phase along the grain boundaries whereas high-temperature strength are reduced due to the lack of the δ phase [48,49]. High-temperature strength can be achieved when the amount of δ phase is about 4% [8]. As it was discussed, the grain growth can be controlled by the δ phase at high temperatures. In addition to the δ phase, the grain boundary migration can be inhibited by MC carbides. However, they can cause intergranular cracking when they precipitate at the grain boundaries [47]. MC carbides were observed at the grain boundaries shown in Fig. 5 and MC carbide coarsening can be seen due to diffusion of Nb from dissolved Laves. Additionally, the brittle Laves should be dissolved to release Nb and Ti elements with the solution heat treatment. Thus, more strengthening phases can be obtained during the subsequent aging treatment [19].

The average hardness values of the solution heat-treated samples increased compared to the AB sample while the area-weighted average grain size values were similar. The precipitated δ phase and strengthening phases (γ" and γ′) can be shown as a reason for this. Huang et al. [21] investigated the effect of solution temperature, time and cooling rate on the IN718 produced by the L-PBF. They did solution heat treatment at 1080 °C for 45 min followed by FC. Their findings are

consistent with the current study. They concluded that the strengthening phases precipitating during FC is relatively small compared to aging. Although these phases increase tensile strength, they will enlarge during the subsequent aging process. Therefore, the strengthening effect will be weakened. Moreover, Tucho et al. [3] reported that 1100 °C for 1 h is not enough to dissolve undesired phases to achieve a complete recrystallization during solution heat treatment. Also, tiny Laves precipitates were found at 1250 °C in their study. It can be assumed that the solution heat-treated samples may have the residual Laves phase in this study. Recently, Gruber et al. [24] reported stress-relief heat treatments at 1065 °C for 1.5 h and 1150 °C for 6 h with FC (6 °C/min). They indicated that most of the grains were non-recrystallized, along with intercellular microsegregation at 1065 °C for 1.5 h. However, they reported complete dissolution of all secondary phases except coarsened primary carbides, along with reduced the macro- and micro-residual stresses at 1150 °C for 6 h. This result differs from our finding because we observed the δ phase at the grain boundaries of the 1150-45 sample. Additionally, Kouraytem et al. [23] carried out recrystallization heat treatment at 1250 °C for 1 h with FC (10.4 °C/min). They observed the δ phase and MC carbide at the grain boundaries and strengthening phases (γ" and γ′) in the matrix, along with dissolving Laves phase into the matrix. The results of the 1250-45 sample are similar to this study.

In addition to the L-PBF process parameters (discussed in section 4.1.), the texture or crystal orientation can also change with the recrystallization which involves recovery and growth of new grains by the migration of high-angle grain boundary. The as built sample has an intense Cube texture {001}//<100>, which is a typical solidification texture for as-built additively manufactured materials with cubic crystal structure. This inherited cube texture is still intense in 1050-15, 1050-45 and 1150-15 samples. The recrystallization fraction does not change significantly for those samples (Table 6); also there is no significant difference in terms of microstructure, grain size, KAM distribution and GND density compared to the AB sample. The 1150-45 sample shows significant reduction in GND density, slight increase in grain size and this sample is 76% recrystallized. The crystallographic texture of 1150-45 sample also changes significantly, the most intense texture component is no longer the cube component, but the first generation cube twin texture {122}<212> becomes intense. This texture component forms due to formation annealing twins and has an <111>60° orientation relationship with the cube texture component. Fig. 9 (c) also shows that the highest twin density is present in 1150-45 sample and this is also evident in EBSD maps showing twin boundaries (Figs. 6(c) and 7(c)). The crystallographic texture also proves the twinning-assisted recrystallization mechanism, which is also seen in L-PBF produced AISI 316 L samples [33]. The recrystallization nuclei then sweep through the high defect density matrix. The samples treated at 1250 °C are almost completely recrystallized. This recrystallization forms a weaker cube texture and much stronger P-orientation, namely {011}<112>, which is typical for FCC materials with intermediate levels of stacking fault energy (SFE). At 1250 °C, the growth of recrystallized grains is very limited, due to the formation of non-coherent precipitates.

5. Conclusions

In this study, the effects of solution heat treatment followed by FC (5 °C/min) with different temperatures (1050, 1150, 1250 °C) and holding times (15, 45, 90 min) were investigated. This study aimed to fill the gap in the literature about the effects of slow cooling during solution heat treatment on the microstructure and texture and hardness of IN718 produced by the L-PBF, along with the recrystallization and grain growth kinetics. The main findings can be summarized as follows:

1) The bowl-shaped melt pools and chessboard-like grain pattern, along with the area-weighted average grain size, KAM and GND density values remained unchanged up to the 1150-15 sample. Although the first recrystallized grains were observed in the 1150-15 sample, a significant microstructural change was observed in the 1150-45 sample. It can be estimated that 1150 °C and 45 min are threshold values for recrystallization temperature and holding time, respectively. The twin boundaries, along with 87.3% grain size increment compared to the AB sample, were observed in the 1150-45 sample. Additionally, the recrystallization was almost completed in the 1250-45 sample, along with 118% grain size increment compared to the AB sample. Moreover, a 39% increment of the twin boundary fraction in the 1250-45 sample compared to the 1150-45 sample.
2) Recrystallization started from the high dislocation density regions such as overlapping regions and the borders of the chessboard-like pattern, and the average GND density values reduced 54% for the 1150-45 sample and 81% for the 1250-45 sample. Most of the residual stresses occurred during the L-PBF process can be reduced with the solution heat treatment temperature of 1250 °C. Moreover, the recrystallization fractions of the 1150-45 and 1250-45 samples were calculated as 0.76 and 0.92, respectively.
3) The δ phase, the strengthening phases (γ" and γ′) and MC carbides were observed in the solution heat-treated samples due to the FC (5 °C/min). Also, these samples may have brittle residual Laves phase.
4) The microhardness of the solution heat-treated samples increased around 20.5–26.6% compared to the AB sample due to the precipitated phases during FC. Therefore, this must be considered for postprocessing operations as higher hardness may induce machining challenges.
5) The as-built sample exhibits cube texture {001}<100>, which transforms into first generation cube-twin texture {122}<212> due to twinning-assisted recrystallization mechanism. Almost no new twins are formed during growth stage, therefore other recrystallization texture components, cube and P-component, both of which are typical for FCC materials with intermediate SFE are formed.

Declaration of Competing Interest

The authors declare that they have no known competing financial interests or personal relationships that could have appeared to influence the work reported in this paper.

Acknowledgments

This publication has emanated from research supported by a research grant from Science Foundation Ireland (SFI) under grant number 16/RC/3872 and is co-funded under the European Regional Development Fund.

The authors are grateful for all equipment support for EBSD from the Metal Forming Center of Excellence at Atılım University.

REFERENCES

[1] Choi JP, Shin GH, Yang S, Yang DY, Lee JS, Brochu M, et al. Densification and microstructural investigation of Inconel 718 parts fabricated by selective laser melting. Powder Technol 2017;310:60–6. https://doi.org/10.1016/j.powtec.2017.01.030.

[2] Panwisawas C, Tang YT, Reed RC. Metal 3D printing as a disruptive technology for superalloys. Nat Commun 2020;11:1–4. https://doi.org/10.1038/s41467-020-16188-7.

[3] Tucho WM, Cuvillier P, Sjolyst-Kverneland A, Hansen V. Microstructure and hardness studies of Inconel 718 manufactured by selective laser melting before and after solution heat treatment. Mater Sci Eng, A 2017;689:220–32. https://doi.org/10.1016/j.msea.2017.02.062.

[4] Zhang D, Feng Z, Wang C, Wang W, Liu Z, Niu W. Comparison of microstructures and mechanical properties of Inconel 718 alloy processed by selective laser melting and casting. Mater Sci Eng, A 2018;724:357–67. https://doi.org/10.1016/j.msea.2018.03.073.

[5] Ozer S, Mert G, Davut K, Esen Z, Dericioglu AF. Effect of post fabrication aging treatment on the microstructure , crystallographic texture and elevated temperature mechanical properties of IN718 alloy fabricated by selective laser melting. J Mater Process Technol 2022;306:117622. https://doi.org/10.1016/j.jmatprotec.2022.117622.

[6] Sanchez S, Smith P, Xu Z, Gaspard G, Hyde CJ, Wits WW, et al. Powder Bed Fusion of nickel-based superalloys: a review. Int J Mach Tool Manufact 2021;165. https://doi.org/10.1016/j.ijmachtools.2021.103729.

[7] Ferreri NC, Vogel SC, Knezevic M. Determining volume fractions of γ, γ′, γ″, δ, and MC-carbide phases in Inconel 718 as a function of its processing history using an advanced neutron diffraction procedure. Mater Sci Eng, A 2020;781:139228. https://doi.org/10.1016/j.msea.2020.139228.

[8] Fayed EM, Saadati M, Shahriari D, Brailovski V, Jahazi M, Medraj M. Effect of homogenization and solution treatments time on the elevated-temperature mechanical behavior of Inconel 718 fabricated by laser powder bed fusion. Sci Rep 2021;11:1–17. https://doi.org/10.1038/s41598-021-81618-5.

[9] Doğu MN, Esen Z, Davut K, Tan E, Gümüş B, Dericioglu AF. Microstructural and texture evolution during thermo-hydrogen processing of Ti6Al4V alloys produced by electron beam melting. Mater Char 2020;168. https://doi.org/10.1016/j.matchar.2020.110549.

[10] Obeidi MA, Monu M, Hughes C, Bourke D, Dogu MN, Francis J, et al. Laser beam powder bed fusion of nitinol shape memory alloy (SMA). J Mater Res Technol 2021;14:2554–70. https://doi.org/10.1016/j.jmrt.2021.07.126.

[11] Balbaa M, Mekhiel S, Elbestawi M, McIsaac J. On selective laser melting of Inconel 718: densification, surface roughness, and residual stresses. Mater Des 2020;193:108818. https://doi.org/10.1016/j.matdes.2020.108818.

[12] Mussatto A, Groarke R, O'Neill A, Obeidi MA, Delaure Y, Brabazon D. Influences of powder morphology and spreading parameters on the powder bed topography uniformity in powder bed fusion metal additive manufacturing. Addit Manuf 2021;38:101807. https://doi.org/10.1016/j.addma.2020.101807.

[13] Dogu MN, McCarthy E, McCann R, Mahato V, Caputo A, Bambach M, et al. Digitisation of metal AM for part microstructure and property control. Int J Material Form 2022;15. https://doi.org/10.1007/s12289-022-01686-4.

[14] Ahmed Obeidi M, Uí Mhurchadha SM, Raghavendra R, Conway A, Souto C, Tormey D, et al. Comparison of the porosity and mechanical performance of 316L stainless steel manufactured on different laser powder bed fusion metal additive manufacturing machines. J Mater Res Technol 2021;13:2361–74. https://doi.org/10.1016/j.jmrt.2021.06.027.

[15] Moussaoui K, Rubio W, Mousseigne M, Sultan T, Rezai F. Effects of Selective Laser Melting additive manufacturing parameters of Inconel 718 on porosity, microstructure and mechanical properties. Mater Sci Eng, A 2018;735:182–90. https://doi.org/10.1016/j.msea.2018.08.037.

[16] Ozsoy A, Yasa E, Keles M, Tureyen EB. Pulsed-mode Selective Laser Melting of 17-4 PH stainless steel: effect of laser parameters on density and mechanical properties. J Manuf Process 2021;68:910–22. https://doi.org/10.1016/j.jmapro.2021.06.017.

[17] Mussatto A, Groarke R, Vijayaraghavan RK, Hughes C, Mcnally PJ, Delaure Y, et al. Assessing dependency of part properties on the printing location in laser-powder bed fusion metal additive manufacturing. Mater Today Commun 2022;30. https://doi.org/10.1016/j.mtcomm.2022.103209.

[18] Cao GH, Sun TY, Wang CH, Li X, Liu M, Zhang ZX, et al. Investigations of γ′ γ″ and δ precipitates in heat-treated Inconel 718 alloy fabricated by selective laser melting. Mater Char 2018;136:398–406. https://doi.org/10.1016/j.matchar.2018.01.006.

[19] Li X, Shi JJ, Wang CH, Cao GH, Russell AM, Zhou ZJ, et al. Effect of heat treatment on microstructure evolution of Inconel 718 alloy fabricated by selective laser melting. J Alloys Compd 2018;764:639–49. https://doi.org/10.1016/j.jallcom.2018.06.112.

[20] Fayed EM, Shahriari D, Saadati M, Brailovski V, Jahazi M, Medraj M. Influence of homogenization and solution treatments time on the microstructure and hardness of Inconel 718 fabricated by laser powder bed fusion process. Materials (Basel) 2020;13. https://doi.org/10.3390/ma13112574.

[21] Huang W, Yang J, Yang H, Jing G, Wang Z, Zeng X. Heat treatment of Inconel 718 produced by selective laser melting: microstructure and mechanical properties. Mater Sci Eng, A 2019;750:98–107. https://doi.org/10.1016/j.msea.2019.02.046.

[22] Shi JJ, Li X, Zhang ZX, Cao GH, Russell AM, Zhou ZJ, et al. Study on the microstructure and creep behavior of Inconel 718 superalloy fabricated by selective laser melting. Mater Sci Eng, A 2019;765. https://doi.org/10.1016/j.msea.2019.138282.

[23] Kouraytem N, Varga J, Amin-Ahmadi B, Mirmohammad H, Chanut RA, Spear AD, et al. A recrystallization heat-treatment to reduce deformation anisotropy of additively manufactured Inconel 718. Mater Des 2021:198. https://doi.org/10.1016/j.matdes.2020.109228.

[24] Gruber K, Dziedzic R, Kuźnicka B, Madejski B, Malicki M. Impact of high temperature stress relieving on final properties of Inconel 718 processed by laser powder bed fusion. Mater Sci Eng, A 2021:813. https://doi.org/10.1016/j.msea.2021.141111.

[25] Gruber K, Stopyra W, Kobiela K, Madejski B, Malicki M, Kurzynowski T. Mechanical properties of Inconel 718

additively manufactured by laser powder bed fusion after industrial high-temperature heat treatment. J Manuf Process 2022;73:642–59. https://doi.org/10.1016/j.jmapro.2021.11.053.
[26] Newell D. Solution anneal heat treatments to enhance mechanical performance of additively manufactured IN718. 2020.
[27] F3055-14a. Standard specification for additive manufacturing nickel alloy (UNS N06625). 2014. p. 1–8. https://doi.org/10.1520/F3055-14A [COPYRIGHT].
[28] Vander Voort GF, Manilova EP. Metallographic techniques for superalloys. Microsc Microanal 2004;10:690–1. https://doi.org/10.1017/S1431927604883442.
[29] Deng D, Peng RL, Brodin H, Moverare J. Microstructure and mechanical properties of Inconel 718 produced by selective laser melting: sample orientation dependence and effects of post heat treatments. Mater Sci Eng, A 2018;713:294–306. https://doi.org/10.1016/j.msea.2017.12.043.
[30] Liu SY, Li HQ, Qin CX, Zong R, Fang XY. The effect of energy density on texture and mechanical anisotropy in selective laser melted Inconel 718. Mater Des 2020:191. https://doi.org/10.1016/j.matdes.2020.108642.
[31] Gokcekaya O, Ishimoto T, Hibino S, Yasutomi J, Narushima T, Nakano T. Unique crystallographic texture formation in Inconel 718 by laser powder bed fusion and its effect on mechanical anisotropy. Acta Mater 2021;212:116876. https://doi.org/10.1016/j.actamat.2021.116876.
[32] Zhang S, Lin X, Wang L, Yu X, Hu Y, Yang H. Strengthening mechanisms in selective laser-melted Inconel718 superalloy. Mater Sci Eng, A 2021;812:141145. https://doi.org/10.1016/j.msea.2021.141145.
[33] Suwas S, Ray RK. Crystallographic texture of materials. 2014. https://doi.org/10.1007/978-1-4471-6314-5_5.
[34] Jiang R, Mostafaei A, Pauza J, Kantzos C, Rollett AD. Varied heat treatments and properties of laser powder bed printed Inconel 718. Mater Sci Eng, A 2019;755:170–80. https://doi.org/10.1016/j.msea.2019.03.103.
[35] Aota LS, Bajaj P, Zilnyk KD, Jägle EA, Ponge D, Sandim HRZ, et al. Recrystallization kinetics, mechanisms, and topology in alloys processed by laser powder-bed fusion: AISI 316L stainless steel as example. Materialia 2021;20:101236. https://doi.org/10.1016/j.mtla.2021.101236.
[36] Holland S, Wang X, Chen J, Cai W, Yan F, Li L. Multiscale characterization of microstructures and mechanical properties of Inconel 718 fabricated by selective laser melting. J Alloys Compd 2019;784:182–94. https://doi.org/10.1016/j.jallcom.2018.12.380.
[37] Holland S, Wang X, Fang XY, Guo YB, Yan F, Li L. Grain boundary network evolution in Inconel 718 from selective laser melting to heat treatment. Mater Sci Eng, A 2018;725:406–18. https://doi.org/10.1016/j.msea.2018.04.045.
[38] Aota LS, Bajaj P, Zilnyk KD, Ponge D, Sandim HRZ. The origin of abnormal grain growth upon thermomechanical processing of laser powder-bed fusion alloys. Materialia 2021;20:101243. https://doi.org/10.1016/j.mtla.2021.101243.
[39] DebRoy T, Wei HL, Zuback JS, Mukherjee T, Elmer JW, Milewski JO, et al. Additive manufacturing of metallic components – process, structure and properties. Prog Mater Sci 2018;92:112–224. https://doi.org/10.1016/j.pmatsci.2017.10.001.
[40] Huang L, Cao Y, Li G, Wang Y. Microstructure characteristics and mechanical behaviour of a selective laser melted Inconel 718 alloy. J Mater Res Technol 2020;9:2440–54. https://doi.org/10.1016/j.jmrt.2019.12.075.
[41] Calandri M, Yin S, Aldwell B, Calignano F, Lupoi R, Ugues D. Texture and microstructural features at different length scales in Inconel 718 produced by selective laser melting. Materials (Basel) 2019;12. https://doi.org/10.3390/ma12081293.
[42] Jin Y, Bernacki M, Agnoli A, Lin B, Rohrer GS, Rollett AD, et al. Evolution of the annealing twin density during δ-Supersolvus grain growth in the nickel-based superalloy Inconel™ 718. Metals (Basel) 2015;6:1–13. https://doi.org/10.3390/met6010005.
[43] Mahajan S, Pande CS, Imam MA, Rath BB. Formation of annealing twins. Ind Heat 2000;67:18.
[44] Mahajan S. Critique of mechanisms of formation of deformation, annealing and growth twins: face-centered cubic metals and alloys. Scripta Mater 2013;68:95–9. https://doi.org/10.1016/j.scriptamat.2012.09.011.
[45] Jin Y, Lin B, Bernacki M, Rohrer GS, Rollett AD, Bozzolo N. Annealing twin development during recrystallization and grain growth in pure nickel. Mater Sci Eng, A 2014;597:295–303. https://doi.org/10.1016/j.msea.2014.01.018.
[46] Mostafa A, Rubio IP, Brailovski V, Jahazi M, Medraj M. Structure, texture and phases in 3D printed IN718 alloy subjected to homogenization and HIP treatments. Metals (Basel) 2017;7:1–23. https://doi.org/10.3390/met7060196.
[47] Gallmeyer TG, Moorthy S, Kappes BB, Mills MJ, Amin-Ahmadi B, Stebner AP. Knowledge of process-structure-property relationships to engineer better heat treatments for laser powder bed fusion additive manufactured Inconel 718. Addit Manuf 2020;31:100977. https://doi.org/10.1016/j.addma.2019.100977.
[48] Yong CK, Gibbons GJ, Wong CC, West G. A critical review of the material characteristics of additive manufactured in718 for high-temperature application. Metals (Basel) 2020;10:1–22. https://doi.org/10.3390/met10121576.
[49] Kuo YL, Horikawa S, Kakehi K. The effect of interdendritic δ phase on the mechanical properties of Alloy 718 built up by additive manufacturing. Mater Des 2017;116:411–8. https://doi.org/10.1016/j.matdes.2016.12.026.